



# Large-eddy simulation of a supercritical channel flow using a shock capturing numerical scheme



Guillaume Ribert<sup>a,\*</sup>, David Taieb<sup>a</sup>, Vigor Yang<sup>b</sup>

<sup>a</sup> CORIA – CNRS, Normandie Université, INSA de Rouen, Technopôle du Madrillet, BP 8, 76801 Saint-Etienne-du-Rouvray, France

<sup>b</sup> Georgia Institute of Technology, School of Aerospace Engineering, Atlanta, GA 30332-0150, USA

## ARTICLE INFO

### Article history:

Received 16 July 2014

Received in revised form 8 April 2015

Accepted 14 May 2015

Available online 22 May 2015

### Keywords:

Large-eddy simulation

Supercritical

Channel flow

Shock capturing

## ABSTRACT

This paper investigates the simulation of supercritical fluids flowing inside small cooling channels. In the context of liquid rocket engines, a strong heat flux coming from the combustion chamber (locally  $\phi \approx 80 \text{ MW/m}^2$  for the Ariane 5 main-engine) may lead to very steep density gradients close to the wall. These gradients have to be thermodynamically and numerically captured to really understand the mechanism of heat transfer from the wall to the fluid. A shock-capturing WENO numerical scheme, usually used with the ideal gas law, was extended to real gases and applied to the simulation of an academic channel flow configuration that uses hydrogen as fluid. Results showed very elongated ligaments in the streamwise direction with a deep penetration in the wall-normal direction. A linear analysis was performed to link the fluctuations of compressibility factor ( $Z'$ ) to temperature fluctuations ( $T'$ ) in the case of an adiabatic and isothermal wall. The usual Strong Reynolds Analogy (SRA) could not be confirmed with real gas effects.  $Z'$  fluctuations was found lower than 1%, thus becoming harder to distinguish the physical fluctuations from the numerical error and a more refine simulation should be require to deliver a definitive conclusion.

© 2015 Elsevier Ltd. All rights reserved.

## 1. Introduction

The ability to model and predict heat transfer of wall-bounded compressible turbulent flows is crucial in the design and optimization of aerospace propellants. In particular, when increasing the thrust efficiency of future liquid rocket engines (LRE), the combustion chamber must operate at very high pressures and temperatures. This requires sufficient cooling to maintain the chamber walls within acceptable temperature limits either to prevent failure or increase cycle life. For instance, the nonlinear deformation of the combustion chamber wall has been studied by Riccius et al. [1] under cyclic thermal and mechanical loading. Regenerative cooling or forced convection cooling are the most common methods used: a cryogenic fuel in a supercritical state, typically  $\text{H}_2$ , flows in small channels embedded in the chamber walls, including the nozzle throat portion, and absorbs the heat from the hot-gas side wall. For such configurations, experiments over the past ten years have shown a significant thermal-load sensitivity to channel size, geometry effects and fluid properties. For example, the use of high aspect ratio (height/width) cooling channels (HARCC) [2,3] is a promising technique to reduce the near wall

combustion chamber temperature for a limited pressure drop. For example, the effect of tube geometry on regenerative cooling performance has been studied by Parris and Landrum [4], and Pizzarelli et al. [5,6] simulated the behavior of supercritical fluids inside heated curved channels in a RANS (Reynolds-Averaged Navier–Stokes) context. They observed the existence of strong fluid recirculation contrary to the straight channel case. According to the authors, there is no large-eddy simulation (LES) of such configuration.

The description of a turbulent flow passing through narrow channels and experiencing a strong heat transfer involving large compressibility effects is still a numerical challenge. Much efforts are then required to put emphasis into the near-wall thermal structures and their impact on the mean velocity and temperature distributions. Based on the wall-normal vorticity contours, Coleman et al. [7] have shown the existence of long and coherent streaks close to the wall and under strong compressibility effects as well as horseshoe-like (HS) structures. These latter are classical structures for channel flow configurations and have already been observed in sub- and super-sonic [8,9] configurations. The HS structure is strongly three-dimensional and is a key-factor of the heat exchange between the cold and the hot parts of flow [10].

In contrast to this very precise analysis, the engineering design of LRE cooling systems requires correlations to predict the heat

\* Corresponding author.

E-mail address: [ribert@coria.fr](mailto:ribert@coria.fr) (G. Ribert).

transfer from the burned gases to the combustion chamber wall, and from the wall to the cooling fluid. Such a study for supercritical hydrogen in regenerative cooling channels has been recently done by Locke and Landrum [11]. Pioro et al. [12] have detailed similar correlations in the context of supercritical water for fossil-fired power plants. Finally, Cheng et al. [13] studied the heat transfer in supercritical water cooled flow channels in the context of nuclear power plant design.

The objective of the present paper is to study the supercritical fluid behavior in a LRE cooling channel by using numerical computations. To achieve this objective a numerical scheme based on WENO (Weighted Essentially Non-Oscillatory) formulation is developed for general fluid flows, i.e. regardless the equation of state. Indeed, such strategy may be crucial to capture the large density gradient that may be found when studying the supercritical fluid flows [14]. Appropriated thermodynamics relations required to deal with real gas effects are also presented in the next section. In Section 3, the channel flow configuration is detailed and results are analyzed. Conclusions are provided in Section 4.

## 2. Thermodynamics and numerical solvers

Simulating a supercritical flow requires a unified treatment of general fluid thermodynamics, valid for the entire state of fluid [15]. For instance, Yang and coworkers [15–19] developed and validated various numerical codes able to simulate different configurations: droplet vaporization, laminar diffusion flames, supercritical fluid injection, mixing, swirl injector, etc. Characteristics of the LES numerical code that were used in the present study may be found in Zong and Yang [19]. Nevertheless, it is useful to note that a preconditioning scheme is applied to simulate either sub- or super-sonic flows and that the spatial discretization is achieved with a fourth-order, central-difference scheme (acronym 4CD) in generalized coordinates. A dual-time-stepping integration technique [15] is used with a standard fourth-order Runge–Kutta scheme to perform the inner-loop pseudo-time integration and a second-order backward difference for the real-time derivative term [20]. To ensure computational stability and to prevent numerical oscillations in regions with steep gradients, a fourth-order scalar dissipation with a total-variation-diminishing switch developed by Swanson and Turkel [21] is used. This strategy may be too dissipative as it will be shown in Section 2.2, and a WENO formulation is derived for general fluids hereafter according to the procedure given by Jiang and Shu [22]. Note that the WENO formulation of Martin et al. [23] allows a dynamic balance between a quasi-full-upwind formulation for steep gradients regions and a quasi-central formulation in smooth regions.

### 2.1. WENO formulation for general fluid flow

Developing a numerical scheme for general fluid flow requires particular attention to partial derivatives due to the numerical stiffness caused by rapid flow property variations. The differential form of the internal energy  $e = e(T, \rho)$  may be expressed as

$$de = \left( \frac{\partial e}{\partial T} \right)_{\rho} dT + \left( \frac{\partial e}{\partial \rho} \right)_{T} d\rho = C_v dT + C_T d\rho, \quad (1)$$

where  $T$  and  $\rho$  are temperature and density, respectively. The differential form of specific enthalpy  $h = e + p/\rho$  is written

$$dh = de + \frac{dp}{\rho} - \frac{p}{\rho^2} d\rho = C_v dT + \left( C_T - \frac{p}{\rho^2} \right) d\rho + \frac{dp}{\rho}, \quad (2)$$

where  $p$  is pressure. Introducing the differential form of temperature  $T = T(p, \rho)$ , Eq. (2) can be written

$$dh = \left[ C_v \left( \frac{\partial T}{\partial \rho} \right)_{\rho} + C_T - \frac{p}{\rho^2} \right] d\rho + \left[ C_v \left( \frac{\partial T}{\partial p} \right)_{\rho} + \frac{1}{\rho} \right] dp. \quad (3)$$

A similar derivation may be done to express the differential form of the specific enthalpy as a function of temperature and pressure. This leads to:

$$dh = \left[ C_v + \left( \frac{\partial \rho}{\partial T} \right)_{\rho} \left( C_T - \frac{p}{\rho^2} \right) \right] dT + \left[ \left( \frac{\partial \rho}{\partial p} \right)_{\rho} \left( C_T - \frac{p}{\rho^2} \right) + \frac{1}{\rho} \right] dp, \quad (4)$$

$$= C_p dT + C_T dp. \quad (5)$$

Introducing  $C_p$  (Eq. (5)) into Eq. (3) leads to the differential form of  $h$ :

$$dh = C_p \left( \frac{\partial T}{\partial \rho} \right)_{\rho} d\rho + \left[ C_v \left( \frac{\partial T}{\partial p} \right)_{\rho} + \frac{1}{\rho} \right] dp, \quad (6)$$

$$= \left( \frac{\partial h}{\partial \rho} \right)_{\rho} d\rho + \left( \frac{\partial h}{\partial p} \right)_{\rho} dp. \quad (7)$$

To capture the steep density gradients that are inherent to supercritical flows, a WENO formulation was adopted. This procedure can be applied to any system of hyperbolic conservation laws after their transformation from physical to characteristic space [22]. The transformation requires a special attention to partial derivatives and thermodynamics laws. To highlight this point, the WENO method for general fluids is described in the context of the scalar one-dimensional advection equation,

$$\frac{\partial W}{\partial t} + \frac{\partial F}{\partial x} = 0, \quad (8)$$

where  $W = [\rho, \rho u, \rho e_t]^T$  is the conservative variables vector.  $F = [\rho u, \rho u^2 + p, (\rho e_t + p)u]^T$  represents the conservative variables flux vector.  $u$  and  $e_t$  are velocity (the velocity components are  $\{u, v, w\}$ ) and specific total energy, respectively. Introducing the vector of primitive variables  $V = [\rho, u, p]^T$  into Eq. (8) leads to:

$$\frac{\partial V}{\partial t} + \tilde{A} \frac{\partial V}{\partial x} = 0, \quad (9)$$

where  $\tilde{A} = M^{-1} A M$  with  $A = B M^{-1}$ . The jacobian matrices  $M = \partial W / \partial V$  and  $B = \partial F / \partial V$  are expressed as,

$$M = \begin{bmatrix} 1 & 0 & 0 \\ u & \rho & 0 \\ \alpha & \rho u & \beta \end{bmatrix}, \quad (10)$$

and

$$B = \begin{bmatrix} u & \rho & 0 \\ u^2 & 2\rho u & 1 \\ u\alpha & \rho e_t + p + \rho u^2 & (\beta + 1)u \end{bmatrix}, \quad (11)$$

where  $\alpha = \partial(\rho e_t) / \partial \rho|_{u,p}$  and  $\beta = \partial(\rho e_t) / \partial p|_{u,\rho}$ . The total energy,  $e_t$ , may be split into a specific internal energy,  $e$ , and a kinetic energy,  $e_c = u^2/2$ :  $e_t = e + e_c$ . The matrix  $A$  is then written as,

$$A = \frac{1}{\beta \rho} \begin{bmatrix} 0 & \beta \rho & 0 \\ \rho(u^2 - \alpha + \beta u^2) & \rho u(2\beta - 1) & \rho \\ -u(\rho \beta e_t + \beta p - \rho u^2 + \rho \alpha) & \beta \rho e_t + \beta p - \rho u^2 & \rho u(\beta + 1) \end{bmatrix}, \quad (12)$$

leading to

$$\tilde{A} = \begin{bmatrix} u & \rho & 0 \\ 0 & u & 1/\rho \\ 0 & \rho\tilde{c}^2 & u \end{bmatrix}. \quad (13)$$

The modified speed of sound is given by:

$$\rho\tilde{c}^2 = \frac{\rho e_t + p - \rho\alpha}{\beta}. \quad (14)$$

Eigenvalues of  $\tilde{A}$  are  $\lambda_1 = u$ ,  $\lambda_2 = u + \tilde{c}$  and  $\lambda_3 = u - \tilde{c}$ ; left eigenvectors are then:

$$V_1 = \begin{bmatrix} 1 \\ 0 \\ -1/\tilde{c}^2 \end{bmatrix}, \quad V_2 = \begin{bmatrix} 0 \\ 1 \\ 1/\rho\tilde{c} \end{bmatrix}, \quad V_3 = \begin{bmatrix} 0 \\ 1 \\ -1/\rho\tilde{c} \end{bmatrix}. \quad (15)$$

$\tilde{A}$  may be expressed with a new set of matrices as  $\tilde{A} = P^{-1}\Lambda P$  where

$$P^{-1} = \begin{bmatrix} 1 & 0 & -1/\tilde{c}^2 \\ 0 & 1 & 1/\rho\tilde{c} \\ 0 & 1 & 1/\rho\tilde{c} \end{bmatrix}, \quad P = \begin{bmatrix} 1 & \rho/2\tilde{c} & -\rho/2\tilde{c} \\ 0 & 1/2 & 1/2 \\ 1 & \rho\tilde{c}/2 & -\rho\tilde{c}/2 \end{bmatrix}, \quad (16)$$

and

$$\Lambda = \begin{bmatrix} u & 0 & 0 \\ 0 & u + \tilde{c} & 0 \\ 0 & 0 & u - \tilde{c} \end{bmatrix}. \quad (17)$$

Eq. (9) is then rewritten as,

$$\frac{\partial z}{\partial t} + \Lambda \frac{\partial z}{\partial x} = 0 \quad \text{with} \quad z = PV, \quad (18)$$

$\tilde{c}$  must be a function of known variables. Starting from  $\rho e_t = \rho e_i + \rho u^2/2$  with  $\rho e_i = \rho h - p$ ,  $\alpha$  and  $\beta$  are expressed as follow:

$$\begin{aligned} \alpha &= \left. \frac{\partial \rho e_t}{\partial \rho} \right|_{u,p} = \left. \frac{\partial (\rho h - p + \rho u^2/2)}{\partial \rho} \right|_{u,p} = \left. \frac{\partial (\rho h - p)}{\partial \rho} \right|_p + \frac{u^2}{2} \\ &= \left. \frac{\partial \rho h}{\partial \rho} \right|_p + \frac{u^2}{2} = h + \rho \left. \frac{\partial h}{\partial \rho} \right|_p + \frac{u^2}{2}, \end{aligned} \quad (19)$$

and

$$\beta = \left. \frac{\partial \rho e_t}{\partial p} \right|_{u,p} = \left. \frac{\partial (\rho h - p + \rho u^2/2)}{\partial p} \right|_{u,p} = \rho \left. \frac{\partial h}{\partial p} \right|_p - 1. \quad (20)$$

The modified speed of sound,  $\tilde{c}^2$  (see Eq. (14)) is then written:

$$\tilde{c}^2 = \frac{-\rho \left( \frac{\partial h}{\partial \rho} \right)_p}{\rho \left( \frac{\partial h}{\partial p} \right)_p - 1}. \quad (21)$$

Introducing the partial derivatives from Eqs. (6) and (7) into Eq. (21) finally leads to

$$\tilde{c}^2 = -\frac{C_p \left( \frac{\partial T}{\partial \rho} \right)_p}{C_v \left( \frac{\partial T}{\partial p} \right)_p} = \frac{C_p}{C_v} \left( \frac{\partial p}{\partial \rho} \right)_T, \quad (22)$$

which represents the classical expression of the speed of sound for general fluid flows.

The above relations are general and valid for any equation of state. Then, the WENO methodology for general fluid keeps a formulation similar to that derived with an ideal gas equation with an exception for the speed of sound evaluation which must use the results of specific real gas thermodynamics. In this study, we used either the fifth-order WENO formulation of Jiang and Shu [22] (acronym WENO5) or the formulation of Taylor et al. [24]

and Martin et al. [23] (WENO5-SOL) which improved the resolution of very fine flow structures. Indeed, the latter exhibited a spectral behavior close to fourth-order Padé schemes and has been tested on an homogeneous isotropic turbulence and a compressible turbulent boundary layer. Its implementation has already been successfully performed and validated by the authors on a shock focusing phenomenon [25] and an isothermal wall-bounded channel flow simulation [10].

Aside from these numerical considerations, the LES code used hereafter follows the recommendations of Meng and Yang [15] for real gas thermodynamics. The Soave–Redlich–Kwong (SRK) equation of state replaces the classical ideal gas law:

$$p = \frac{\rho RT}{W - b\rho} - \frac{a}{W} \frac{\rho^2}{(W + b\rho)}. \quad (23)$$

$R$  is the universal gas constant and  $W$  the molecular weight of the fluid mixture. The two parameters,  $a$  and  $b$ , take into account the effect of attractive and repulsive forces among molecules, respectively. Without species mixing,  $a$  and  $b$  are expressed as

$$a = 0.42747 \frac{R^2 T_{c_k}^2}{p_{c_k}} \alpha_k, \quad b = 0.086664 \frac{RT_{c_k}}{p_{c_k}}, \quad (24)$$

for the SRK equation of state.  $T_{c_k}$ ,  $p_{c_k}$  are the critical temperature and pressure for species  $k$ , respectively.  $\alpha_k$  is a function depending on species and temperature. Only the species hydrogen is considered in this study and Graboski and Dauber [26,27] propose to use  $\alpha_k = 1.202 \exp(-0.30228T/T_{c_k})$ . Finally, classical techniques used to evaluate transport properties (viscosity and thermal conductivity) were replaced by accurate high-pressure relations proposed by Chung et al. [28], which extends the Chapman–Enskog theory by introducing a dense-fluid correction.

## 2.2. WENO validation

As already stated above, the numerical code used in this study has been largely validated. To confirm the WENO implementation, all other things being equal, two test-cases were defined: (1) a temperature slot defined by 10 mesh points and (2) a temperature distribution following a quasi-sinus function expressed as  $T = 300 + 400 \times (1 + \cos[2\pi(x - 0.00175)/0.001])$ . Both test-cases were purely convected in a subsonic manner (see Table 1). In Fig. 1(a), a slot of 400 K was convected at a standard pressure. As expected, the WENO dissipation occurred only for discontinuities but still kept three mesh points to describe the plateau of the slot in the present case. The 4CD numerical scheme exhibited a much more dissipative behavior as the slot was spread over 23 mesh points instead of the 17 mesh points required with the WENO formulation; the slot magnitude is not preserved anymore. In Fig. 1(c) and (d), the pressure and temperature ranges changed (see Table 1). The previous observations were recovered for both numerical schemes: the base of the slot was better described with the shock-capturing numerical scheme than with the central numerical scheme with artificial viscosity, regardless of the pressure (up to 10.0 MPa) or temperature. Finally, the convection of the sinus function (Fig. 1(b)) led to a similar behavior of the two schemes, with the exception of the upper part of the results, which exhibited a slight loss of magnitude for the 4CD numerical scheme.

**Table 1**  
Test-cases characteristics of code validation.

Figures	Type	$T_{min} - T_{max}$ (K)	$P_0$ (bar)	$U_0$ (m s <sup>-1</sup> )
Fig. 1(a)	Slot	300–700	1	50
Fig. 1(b)	Sinus	300–1100	100	50
Fig. 1(c)	Slot	300–700	100	50
Fig. 1(d)	Slot	170–300	70	50

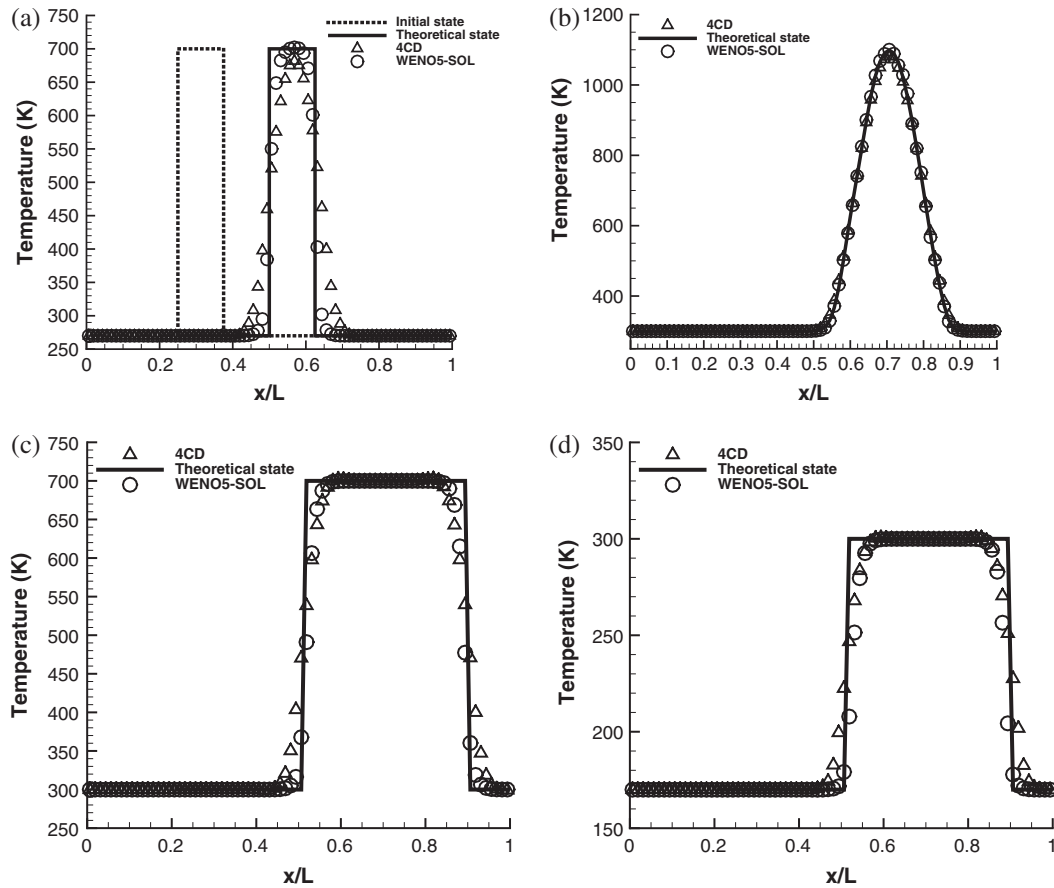


Fig. 1. Comparison between 4CD and WENO5 numerical scheme on temperature slot and sinus convection. The mesh has 360 points. See Table 1 for details.

### 3. Channel flow simulation

Rocket-like cooling channels have been experimentally studied at the DLR facility through the EH3C (Electrically Curved Cooling Channel) test bench [29–31]. A supercritical fluid flows inside a curved or straight channel and experiences a strong heat transfer only coming from one side of the channel wall. The wall heat flux (up to  $20 \text{ MW/m}^2$ ) is imposed by a large bloc of copper electrically heated thus enforcing the temperature on one side of the channel wall. The channel length is 188 mm but the inlet diameter is different from the channel diameter. A converging section is then required but strongly modifies the flow field. Indeed, Torres et al. [31] have shown that a recirculation zone perturbs the first third part of the channel at least. This configuration is then a challenge to simulate [32] and a more academic numerical test-case deriving from this experiment is now studied.

The target configuration (see Fig. 2) is a stream of pure hydrogen flowing between two walls, one exposed to an imposed hot temperature ( $T_w$  at bottom-wall), similarly to the EH3C configuration, and the other one being adiabatic (top-wall). The initial pressure was set above the species critical pressure. A condition of no-slip wall was prescribed on the  $z$ -direction and a periodic boundary was applied for the  $y$ -direction. The bulk velocity was  $u_{max} = 116 \text{ m s}^{-1}$  as in the EH3C configuration leading to an inlet Mach number close to 0.15 (or 0.07 if the wall temperature ( $T_w$ ) is considered). The channel lengths were  $L_x = 20 \text{ mm}$ ,  $L_y = 5 \text{ mm}$  and  $L_z = 2 \text{ mm}$ . Around 10.7 millions of cells were used on 96 processors. The non-reflecting boundary conditions proposed by Poinot and Lele [33] have been applied to the outflow boundary condition, along with the specification of a reference pressure

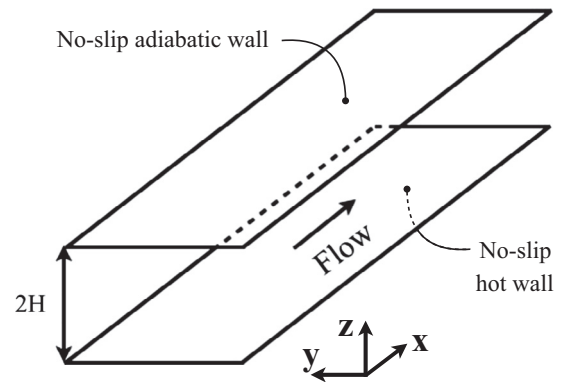


Fig. 2. Sketch of the physical domain under study.

following the procedure given by Zong et al. [34], i.e. in conjunction with a preconditioning scheme for the conservative equations and a dual-time-stepping integration technique [20].

Hydrogen fluid was examined and its operating conditions are summarized in Table 2. The proposed thermal conditions ensured a constant difference of temperature equal to 440 K between the two walls and a compressibility factor of 0.65 and 1 at the upper and bottom walls, respectively. The thermal conditions are imposed through the  $k$  available ghost cells (superscript  $gh$ ) of the numerical code:  $T^{gh}(1-k) = 2T_w - T(k)$ ,  $k = 1, 3$ . The inlet velocity profile used in this study is a classical fully developed channel profile: the average profile of the inlet velocity  $\langle u \rangle (= u - u')$  and the shear stress  $\langle u'w' \rangle$  are shown in Fig. 3.

**Table 2**

Thermodynamic conditions: critical ( $P_c$ ) and initial ( $P_0$ ) pressures are given in bar, critical ( $T_c$ ), initial ( $T_0$ ) and wall ( $T_w$ ) temperatures are given in Kelvin; the initial ( $\rho_0$ ) and wall ( $\rho_w$ ) densities are given in  $\text{kg m}^{-3}$ ; the conductivity at the bottom wall ( $\lambda_w$ ) is in  $\text{W/(m K)}$ .

Fluid	$P_c$	$T_c$	$P_0$	$T_0$	$\rho_0$	$T_w$	$\rho_w$	$\lambda_w$
H <sub>2</sub>	12.9	33.14	40	40	46.7	480	1.98	0.27315

Turbulence was initiated and injected through Klein's algorithm [35] where the correlation length was equal to four local mesh cells. This technique was based on the use of the Reynolds tensor and a digital filter to produce a well correlated turbulence compared to a turbulence generated from white noise. The Smagorinsky model [36] was used with the classical LES formulation [19]. The turbulent Prandtl number ( $Pr_t$ ) was set to 0.81.

### 3.1. Preliminary results

The friction Reynolds number,  $Re_\tau$ , is a key parameter for channel flows description. It is defined based on friction velocity,  $u_\tau$ , as

$$Re_\tau = \frac{\rho_w u_\tau H}{\mu_w} \quad \text{with} \quad u_\tau = \sqrt{\tau_w / \rho_w} \quad \text{where} \quad \tau_w = \mu_w \left. \frac{\partial u}{\partial z} \right|_w. \quad (25)$$

Subscript  $_w$  denotes the wall values.  $^+$  represents the wall unit:

$$z^+ = \frac{z Re_\tau}{H}, \quad (26)$$

where  $H$  is the channel half-width. In this study, different thermal conditions are prescribed for the two walls leading to different values for  $Re_\tau$ . They are all summarized in Table 3 as well as the wall heat flux ( $\Phi_w$ ). In Table 4 the normalized streamwise, spanwise and wall-normal lengths are specified with the mesh discretization for the top and bottom wall, in wall units. Since turbulence requires enough space to be fully developed, the spanwise extension must be chosen carefully. Jimenez and Moin [37] gave the following recommendations to ensure that turbulence is adequately developed:  $L_x^+ = 300$  and  $L_z^+ = 100$  (with  $L_i^+ = L_i Re_\tau / H$ ) meaning that our domain is *a priori* well-dimensioned. Indeed, in the present study,  $L_x^+ = 18,000$  and  $L_z^+ = 1800$ . These values were obtained with the lowest  $Re_\tau$  value occurring at the bottom hot wall.

This point must also be checked, *a posteriori*, by studying the autocorrelation functions of representative flow field fluctuations as pressure. Indeed real gas effects and synthetic turbulent injection may have a strong impact on the flow field. An optimal dimension is obtained when the different fluctuations become uncorrelated before the half of the domain extension. The two-point correlation function of any variables,  $\alpha$ , is given by:

$$R_{\alpha\alpha}(x) = \frac{\langle \alpha(x_{ref}) \alpha(x_{ref} + x) \rangle}{\langle \alpha(x_{ref})^2 \rangle},$$

where  $\langle \alpha \rangle$  is the averaging in the homogeneous normal direction. The two-point correlation functions  $R_{u'u'}$ ,  $R_{p'p'}$  and  $R_{v'v'}$ , were plotted in Fig. 4(a)–(c).  $u'$  and  $v'$  are the  $x$  and  $z$  axis components of the velocity fluctuations, respectively.  $p'$  corresponds to pressure fluctuations.  $R_{u'u'}$  was plotted at the channel center because of the presence of largest coherent structures. In Fig. 4(a)  $R_{u'u'}/R_{u'u'}(0) < 20\%$  for  $x/L_x \approx 0.3$ , meaning that  $u'$  was quickly uncorrelated. In Fig. 4(b)  $R_{p'p'}/R_{p'p'}(0) < 20\%$  for  $x/L_x \approx 0.4$ , showing that the influence of the turbulence inlet injection disappears when half of the domain is reached. The spanwise two-point correlation,  $R_{v'v'}$ , was then considered for the second half of the channel length only (see Fig. 4(c)).  $R_{v'v'}$  became uncorrelated for  $y/L_y \approx |0.2|$ . This channel flow configuration was then well-designed, as enough

space was left in the streamwise and spanwise directions. As a consequence the subsequent results will be considered starting at 80% of the domain, *i.e.* from  $L'_x = 4L_x/5$  to  $L_x$ , to ensure the development of the right channel flow turbulence. A new reference time was then defined as  $T' = L'_x/U_{max}$ . The time left to establish the flow was  $T_{esta} = 10T' = 0.34$  ms and the time left to collect statistics was  $T_{stat} = 20T' = 0.68$  ms.

### 3.2. Results

A classical channel flow profile is observed for the mean profile of velocity (Fig. 5) and the velocity fluctuations, (Fig. 5(e)). However, as there was a difference of temperature between the upper and bottom walls, the maximum of fluctuation was not located at the same distance to the wall in the physical space. Indeed, assuming a peak location at  $z^+ = 10$ , the distance to the wall was given by  $z = z^+ H / Re_\tau$  in the physical location, *i.e.* closer to the wall when  $Re_\tau$  increased. As a consequence, the peak of velocity fluctuations were closer to the wall when located at the top-wall than at the bottom-wall.

Defining the non-dimensional mean temperature,  $T^*$ , as

$$T^* = \frac{\bar{T} - T_0}{T_w - T_0}, \quad (27)$$

the partial derivative of  $T^*$  with  $z$  is linked to the wall heat flux as

$$\left. \frac{\partial T^*}{\partial z} \right|_w = \frac{1}{T_w - T_0} \left. \frac{\partial (\bar{T} - T_0)}{\partial z} \right|_w = \frac{\Phi_w}{\lambda_w \Delta T}, \quad (28)$$

where  $\Delta T$  was the temperature difference between the hot wall and the inlet fluid ( $\Delta T = 440$  K according to Table 2). For any variable  $\phi$ ,  $\bar{\phi}$  denotes the local averaged value.  $T^* = 1$  corresponded to a fluid temperature equal to the hot wall temperature.  $T^* = 0$  corresponded to a fluid temperature equal to the cold wall temperature, *i.e.* the inlet temperature, as this wall had adiabatic boundary conditions. In Fig. 5(c)  $T^*$  was plotted with a semi-logarithmic scale used for the reduced  $z$ -axis ( $z/H$ ), highlighting the near wall heat flux had changed due to the physical fluid properties. A quite flat profile is noticed when  $z/H \rightarrow 0$  meaning that the heat transfer occurred on a thick fluid layer. This point was also observed in Fig. 6(a) where very elongated ligaments appeared in the streamwise direction with a deep penetration in the wall-normal direction. The normalized root mean square temperature ( $T_{RMS}/T_w$ ) was plotted in Fig. 5(d) with a semi-logarithmic scale to highlight the area of interest. As expected, the maximum temperature fluctuations are close to the bottom wall, where heat transfer occurred between the hot wall and the incoming fluid. At the upper adiabatic wall ( $z/H = 2$ ), temperature fluctuations were almost zero. The peak of magnitude of fluctuations was found around 5% of  $T_w$  near the wall, then decreasing to a lower value of 3% when  $z/H = 0.1$ .

In Fig. 5(c), for  $z/H \in [0.04, 0.4]$ ,  $T^*$  exhibited a single profile that corresponded to a transition zone between the near-wall behavior and the center-channel. This was also observed with the compressibility factor,  $Z$  (see Fig. 5(b)), defined as

$$Z = \frac{p}{\rho r T}, \quad (29)$$

where  $r$  is the specific gas constant. This gradient is almost constant on the whole interval. In Fig. 5(b) the compressibility factor is almost equal to unity at the bottom wall suggesting that real gas effects may not occur. However, in the channel core the compressibility factor was away from unity and the fluid should exhibit some real gas effects.

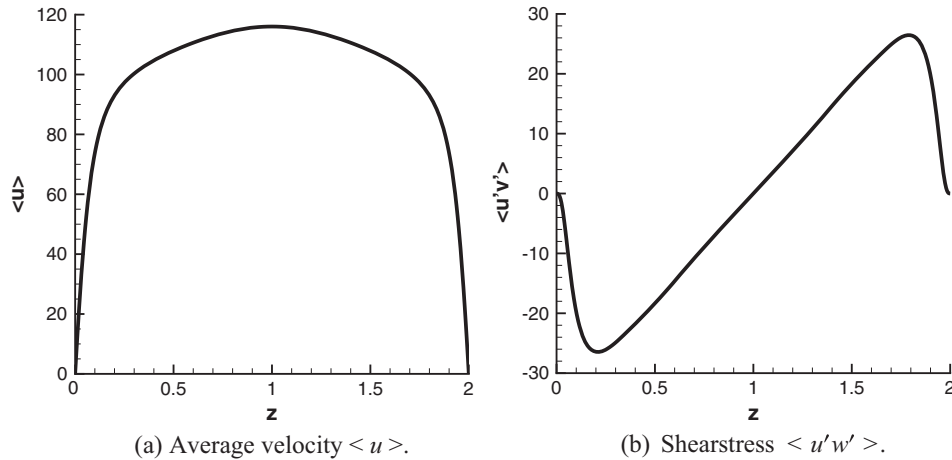


Fig. 3. Inlet velocity profile with Klein's algorithm.

**Table 3**  
Friction Reynolds number ( $Re_\tau$ ) and wall heat flux ( $\Phi_w$ ).

Fluid	$Re_\tau(z=0)$	$Re_\tau(z=2H)$	$\Phi_w$ (MW/m <sup>2</sup> )
H <sub>2</sub>	900	8000	5.45

### 3.3. Scatter-plots

Observations made with the previous flow field analysis may also be understood through the scatter-plots of aerodynamic and thermodynamic variables. Morkovin [38] proposes to link the temperature and velocity fluctuations (called Strong Reynolds Analogy (SRA)) as

$$\frac{T'/\bar{T}}{(\gamma-1)\bar{M}^2 u'/\bar{u}} \approx 1 \quad \text{with} \quad \bar{M} = \bar{u}/\bar{c}, \quad (30)$$

$\gamma$  is the heat capacity ratio and  $M$  is the Mach number. Eq. (30) has been modified by many authors such as [39,40] or [41] to take into account the non-adiabaticity of the wall:

$$\frac{T'/\bar{T}}{(\gamma-1)\bar{M}^2 u'/\bar{u}} \approx \frac{1}{\alpha(\partial\langle T_0 \rangle/\partial\langle T \rangle - 1)}, \quad (31)$$

where  $\partial\langle T_0 \rangle/\partial\langle T \rangle$  corresponds to the differential coefficient of the mean stagnation temperature ( $\langle T_0 \rangle$ ) function of the mean static temperature ( $\langle T \rangle$ ). Depending on the authors, the coefficient  $\alpha$  has different values:

$$\alpha_{Caviglio} = 1, \quad \alpha_{Rubesin} = 1.34 \quad \text{or} \quad \alpha_{Huang} = Pr_t. \quad (32)$$

Rubesin [40] also proposed that pressure and density fluctuations are related by a turbulence modelling parameter,  $n$ , as:

$$\frac{p'}{\bar{p}} = n \frac{\rho'}{\bar{\rho}} = (n-1) \frac{\rho T'}{\bar{\rho} \bar{T}}. \quad (33)$$

If the fluid behaves in a polytropic manner, then  $n$  can be identified as the polytropic coefficient. Coleman et al. [7] (see also [10]) showed on a supersonic compressible channel flow with isothermal walls that close to the wall, temperature and density fluctuations exhibited a linear correlation with  $n$  approaching zero. In the

channel center, temperature and density fluctuations tend to be uncorrelated, i.e.  $n \approx 1$ . All these studies and derivations have been conducted with the ideal gas assumption and equation of state ( $p = \rho RT/W$ ). However, in the present case, the compressibility factor is different from unity and real gas effects must be considered. Indeed, the fluid flows at low temperature and high pressure i.e. in a supercritical state ( $Z \neq 1$ ), and then may change the usual behavior encountered with the ideal gas assumption.

The fluctuations used for the following scatter-plots are taken at  $z^+ = 10$  and correspond to the classical location of the velocity fluctuations peak. In Fig. 7 the near-wall behavior of the fluid was studied through the scatter plots of normalized velocity fluctuations as a function of normalized temperature fluctuations. Near the adiabatic wall (Fig. 7(a)), we observed dispersed results and no link between velocity and temperature fluctuations were found; as a result the SRA cannot be confirmed. Indeed, because of Eq. (30) a linear behavior should be observed as in the work of Brun et al. [42] who simulated an ideal gas compressible channel flow. However, near the hot wall (Fig. 7(b)), the hydrogen fluid exhibited a behavior similar to those observed with ideal gas assumptions ( $Z \approx 1$ ). The coefficient  $\alpha$  in Eq. (31) was close to  $-1$  showing an energy exchange between the wall to the incoming fluid.

In Fig. 8, the normalized density fluctuations were plotted as a function of the normalized temperature fluctuations. A linear correlation was found at the top adiabatic wall (Fig. 8(a)) similarly to observations made by Rubesin [40] for an ideal gas. This assumption can be used presently even if the fluid was experiencing a compressibility factor of  $Z_{z=2H} = 0.65$  because fluctuations of  $Z$  are null. At the bottom wall, this behavior does not hold anymore and the  $\rho' - T'$  relationship becomes more complex (Fig. 8(b)). Indeed, the large heat flux coupled with the non-linear equation of state highly modifies the relationship between the temperature and density fluctuations. As a consequence Eq. (33) is no longer valid and should be closer to a quadratic function.

Scatter-plots of pressure-temperature fluctuations are given in Fig. 9. Close to the adiabatic wall, Fig. 9(a), pressure fluctuations exhibit dispersed values difficult to analyze when function of temperature fluctuations. A similar conclusion can be drawn for the

**Table 4**  
Characteristics lengths and mesh discretization in wall unit. Left (resp. right) part of the table is computed with the values obtained at the bottom (resp. top) wall.

Fluid	$L_x^+$	$L_y^+$	$L_z^+$	$\Delta x^+$	$\Delta y^+$	$\Delta z^+$	$L_x^+$	$L_y^+$	$L_z^+$	$\Delta x^+$	$\Delta y^+$	$\Delta z^+$
H <sub>2</sub>	18,000	4500	1800	32	35	3.42	160,000	40,000	16,000	280	310	30

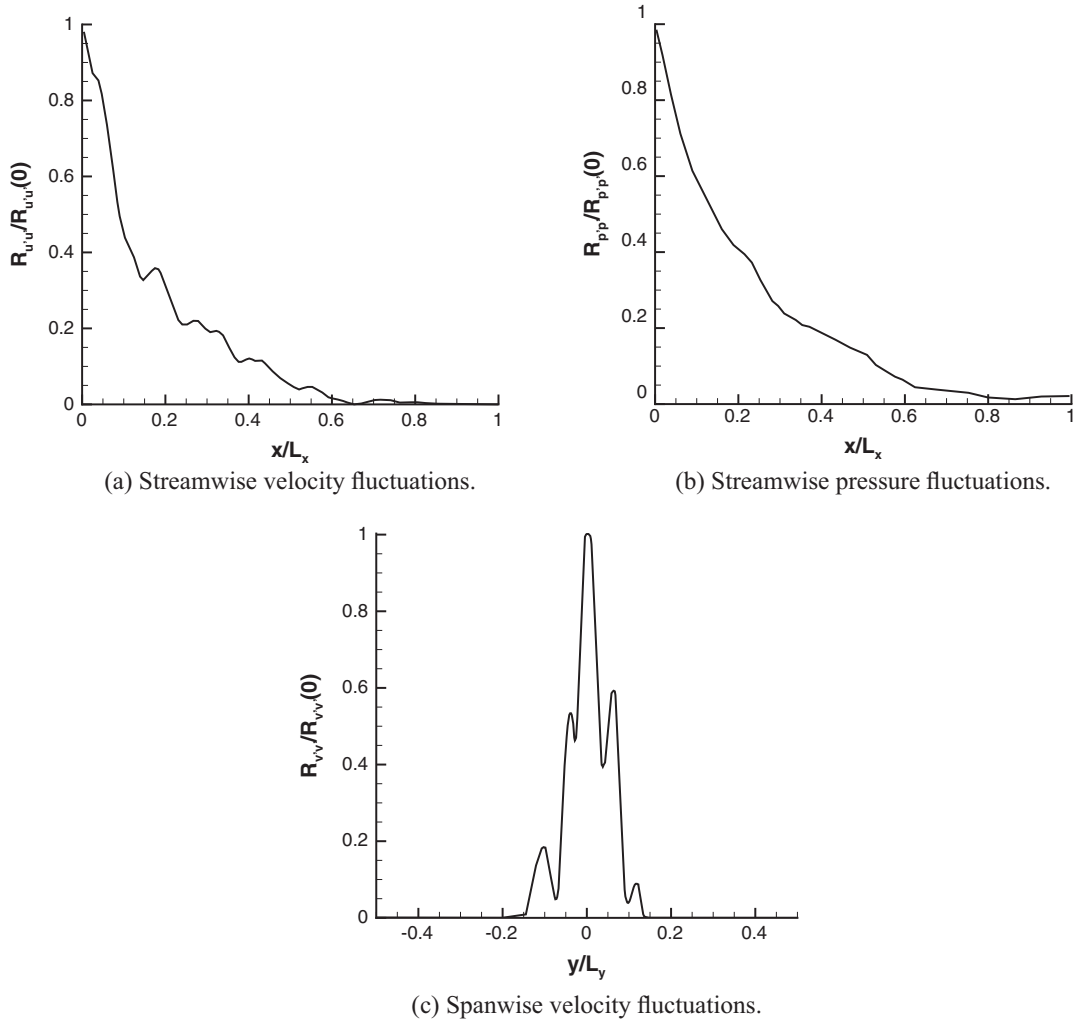


Fig. 4. Two-point correlation plots.

hot wall, Fig. 9(b), suggesting a weak correlation between these two variables. Finally, the magnitude of fluctuations was less than 1%.

In the case of supercritical conditions, the study of the compressibility factor can bring additional information on  $Z$  fluctuations,  $Z'$ , that can potentially be analytically predicted. Starting from Eq. (29),  $Z'$  are expressed as:

$$Z' = \left(\frac{p}{\rho T}\right)' \rightarrow \frac{Z'}{Z} = \frac{p'}{p} - \frac{\rho'}{\rho} - \frac{T'}{T}. \quad (34)$$

- In the case of the adiabatic top wall, a linear correlation between the fluctuations of density,  $\rho'$ , and temperature,  $T'$ , can be found according to Fig. 8(a):  $\rho'/\rho = \alpha_\rho T'/T$ . In addition, assuming a weak linear dependency of pressure fluctuations with temperature fluctuations as  $p'/p = \alpha_p T'/T$ , Eq. (34) can be recast as

$$\frac{Z'}{Z_0} = (\alpha_p - \alpha_\rho - 1) \frac{T'}{T_0} = \alpha_z \frac{T'}{T_0}, \quad (35)$$

with  $\alpha_p$  and  $\alpha_\rho$  two constant coefficients. A least square analysis of the different scatter-plots was realized where linear correlations were found for Figs. 8(a), 9(a) and 10(a). The coefficients  $\alpha$  of Eq. (35) are summarized in Table 5. The coefficient  $\alpha_z$  that

links  $Z$  fluctuations to temperature fluctuations may be deduced either from Eq. (35) with  $\alpha_z^{Eq} = \alpha_p - \alpha_\rho - 1$ , or from scatter-plots values,  $\alpha_z^{Fig}$  (see Fig. 10(a)). In Table 5, a very good agreement was found. With the above decomposition of  $Z'$ , the balance between the different fluctuations can be easily studied considering a unity reference for the temperature fluctuation. In the present case, density fluctuations mainly contributed to  $Z$  fluctuations.

To avoid the assumption on the  $p' - T'$  linear dependency, the compressibility factor may be viewed as

$$Z = \frac{W}{W - b\rho} - \frac{a\rho}{RT(W + b\rho)}, \quad (36)$$

when introducing Eq. (29) into Eq. (23). Using the logarithmic differential, a new expression for  $Z'$  was found:

$$\frac{Z'}{Z} = \frac{\rho'}{\rho} \left[ b\rho \left( \frac{1}{W - b\rho} + \frac{1}{W + b\rho} \right) - 1 \right] - \frac{a'}{a} + \frac{T'}{T}, \quad (37)$$

with  $a'/a$  expressed as  $a'/a = (-0.30228T/T_c) T'/T = \mathcal{A}_k T'/T$ . As the linear relationship between density and temperature fluctuations (see Fig. 8(a)) still hold, Eq. (37) was then rearranged to

$$\frac{Z'}{Z} = \left( \alpha_\rho \left[ b\rho \left( \frac{1}{W - b\rho} + \frac{1}{W + b\rho} \right) - 1 \right] + 1 - \mathcal{A}_k \right) \frac{T'}{T}, \quad (38)$$

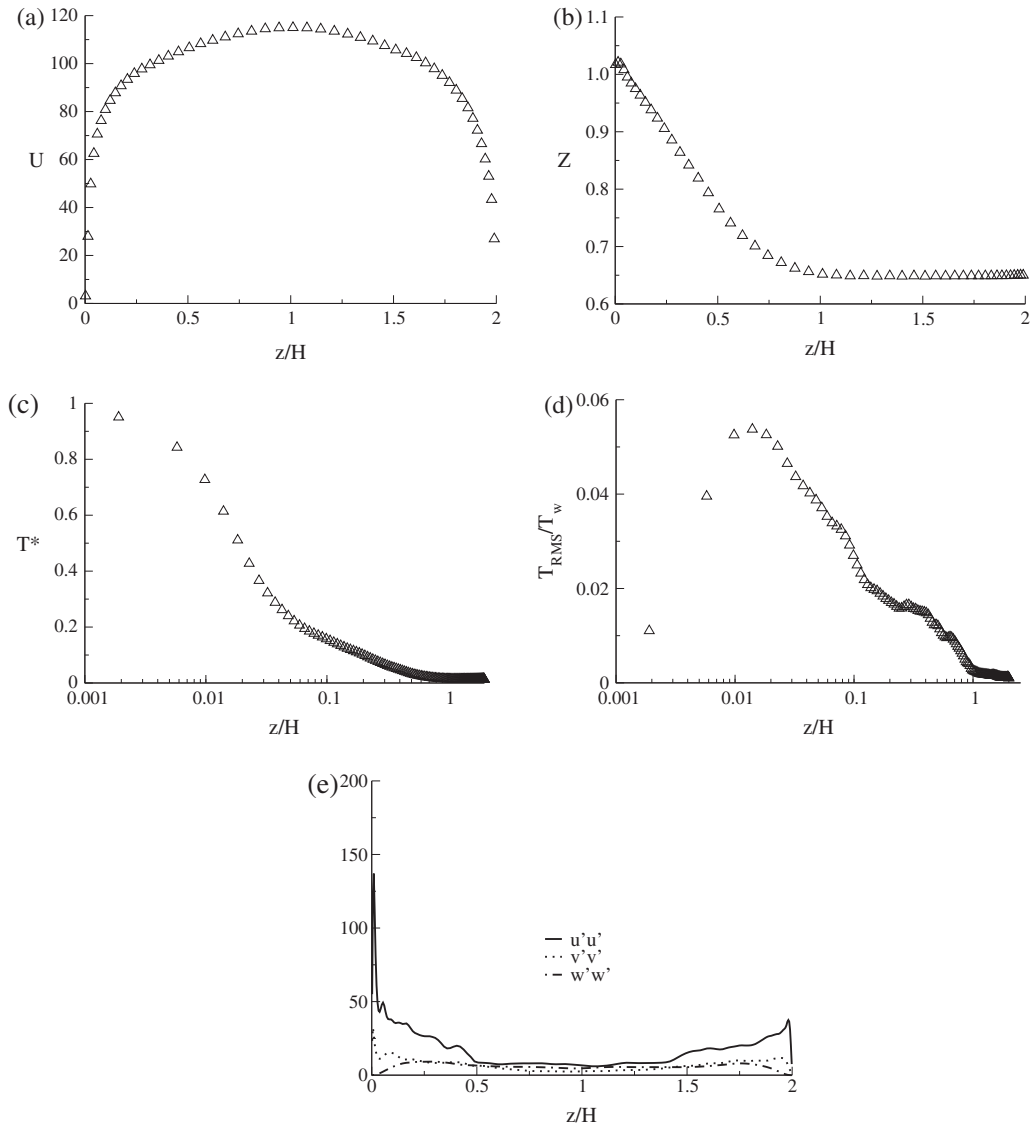


Fig. 5. Mean profiles of (a) velocity, (b) compressibility factor, (c) normalized temperature, (d) normalized temperature fluctuations, (e) velocity fluctuations. Profiles are taken at  $x/H = 9L_x/10$ .

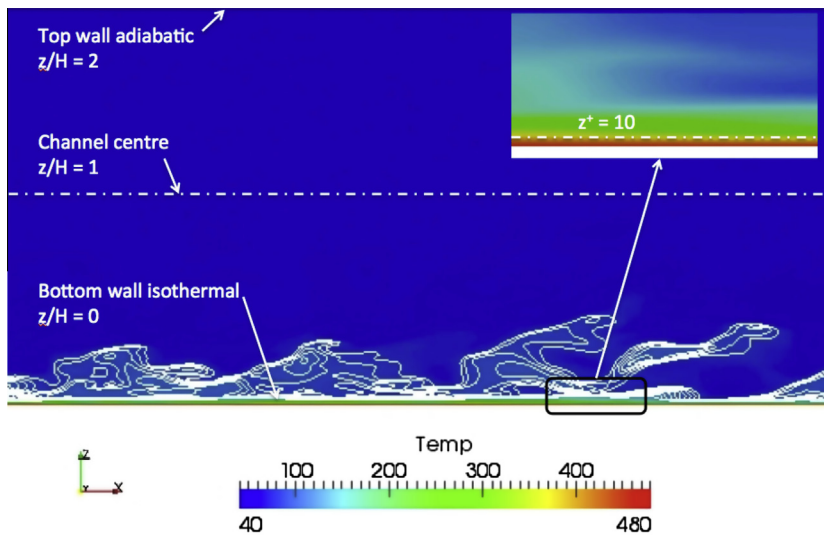


Fig. 6. Fluid flow topology. Only the useful part of the channel length is plotted ( $L'_x$  to  $L_x$ ).

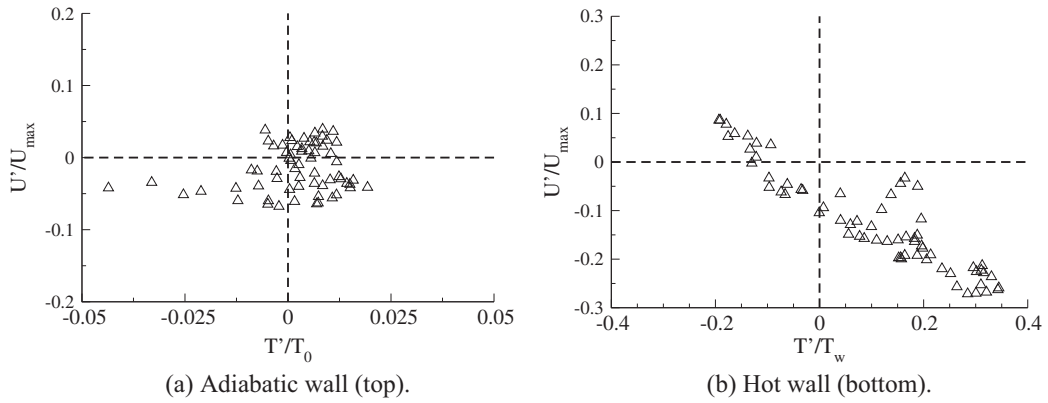


Fig. 7. Scatter plots of temperature and streamwise velocity fluctuations. Missing data are given in Table 2.

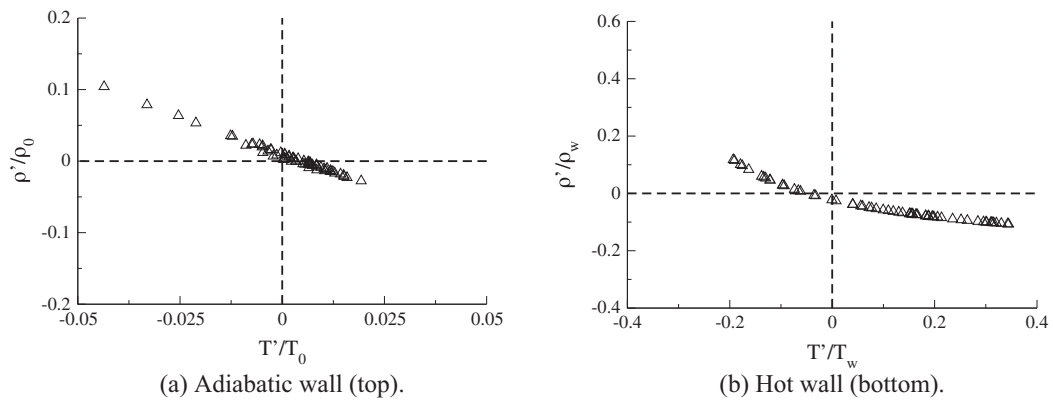


Fig. 8. Scatter plots of temperature and density fluctuations. Missing data are given in Table 2.

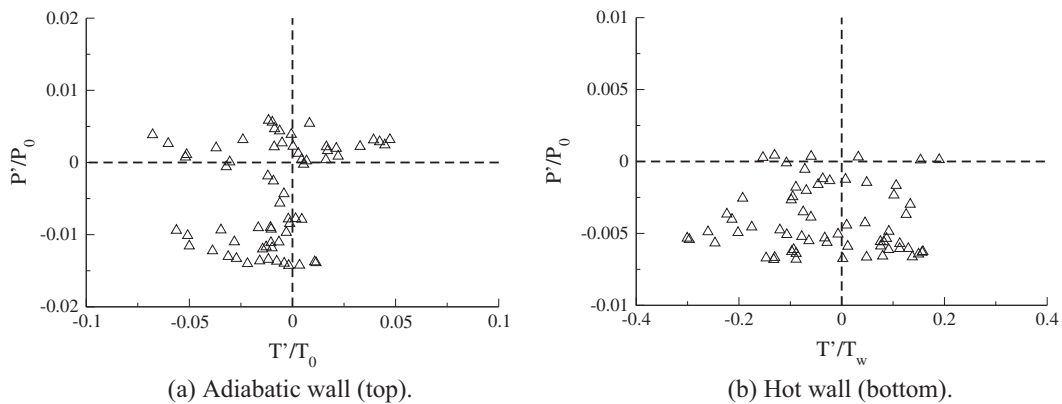


Fig. 9. Scatter plots of temperature and pressure fluctuations. Missing data are given in Table 2.

introducing  $\alpha_\rho$ . The  $L^2$ -norm of the relative error between the  $Z$  fluctuations coming from computations (i.e. Fig. 10) and Eq. (38) was lower than 3% leading to a good approximation for  $Z'$  with a simple linear model.

- In the case of the isothermal bottom hot wall, the above derivation (Eq. (37)) still hold but the relation linking density and temperature fluctuations followed a 3rd order polynomial:  $\rho'/\rho = -1.6969813r_T^3 + 1.1420234r_T^2 - 0.4372111r_T - 0.0230281$ , with  $r_T = T'/T_w$ . As a consequence,  $Z$  fluctuations as a function of

temperature fluctuations (Fig. 10(b)) showed a more complex behavior than a linear evolution (Fig. 10(a)) that was close to a polynomial profile:  $Z'/Z_w = -0.98140838r_T^4 + 0.61594076r_T^3 - 0.11756574r_T^2 - 0.00824721r_T + 0.00440392$ .

Finally, note that the magnitude of  $Z$  fluctuations was lower than 1%, thus becoming harder to distinguish the physical fluctuations from the numerical error. A more refine simulation is then required to further analyze this flow behavior.

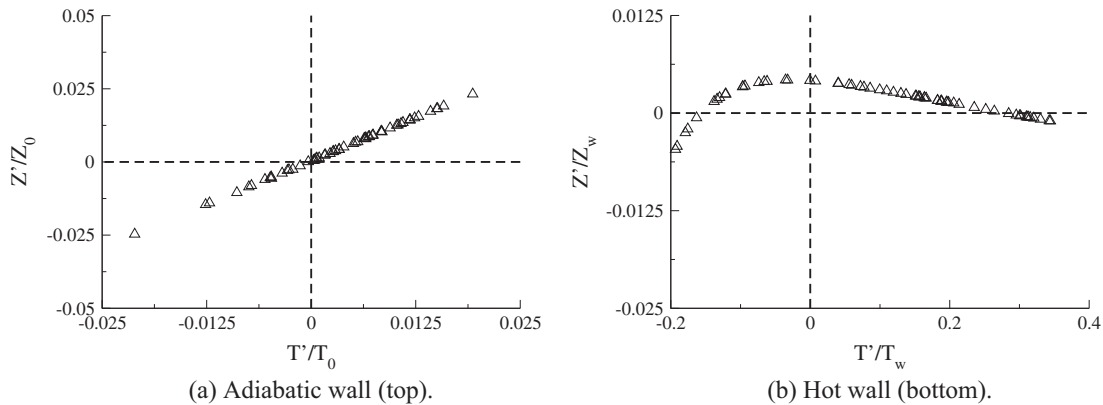


Fig. 10. Scatter plots of temperature and compressibility factor fluctuations. Missing data are given in Table 2.

Table 5

Linear coefficients ( $\alpha_p$ ,  $\alpha_\rho$ ,  $\alpha_z^{Fig}$ ) obtained by a least square analysis of the different scatter-plots for the adiabatic wall. Expected value given by the equation of state analysis:  $\alpha_z^{Eq}$  (to compare with  $\alpha_z^{Fig}$ ).

Species	$\alpha_p$	$\alpha_\rho$	$\alpha_z^{Fig}$	$\alpha_z^{Eq}$
H <sub>2</sub>	0.063	-1.998	1.144	1.061

#### 4. Conclusion

Simulating a fluid flowing in a channel configuration under supercritical conditions and experiencing a strong heat transfer is a numerical challenge. To achieve this objective, a WENO formulation has been extended with success to real gas. The new derivation is similar to the one used with the ideal gas assumption but with thermodynamic characteristics coming from real gas formulation. Its integration into a LES code has been validated against simple test-cases then used to simulate a channel flow configuration. The sharp density gradients that are inherent to supercritical fluid flows are well captured with the real gas WENO formulation. The hydrogen channel flow pattern exhibits long structures with a deep penetration in the wall-normal direction. Scatter-plots revealed that the Strong Reynolds Analogy may not be applied for fluids experiencing real gas effects. For the adiabatic wall a linear analysis was successfully completed to express the fluctuations of the compressibility factor as a function of temperature fluctuations. However, for the isothermal hot wall, a finer simulation is required to yield a similar analysis even if scatter-plots shown a clear polynomial dependency of  $Z'$  on  $T'$ .

A new efficient numerical tool is under development [43,44] in order to study the wall heat transfer with a higher mesh resolution.

#### References

- [1] Riccius J, Haidn O, Zametaev E. Influence of time dependent effects on the estimated life time of liquid rocket combustion chamber walls. In: 40th Joint propul conf (Florida, USA). AIAA 2004-3670; 2004.
- [2] Suslov D, Woschnak J, Sender J, Oschwald M. Test specimen design and measurement technique for investigation of heat transfer processes in cooling channels of rocket engines under real thermal conditions. In: 39th Joint propul conf (Alabama, USA). AIAA 2003-4613; 2003.
- [3] Woschnak A, Suslov D, Oschwald M. Experimental and numerical investigations of thermal stratification effects. In: 39th Joint propul conf (Alabama, USA). AIAA 2003-4615; 2003.
- [4] Parris D, Landrum D. Effect of tube geometry on regenerative cooling performance. In: 41st Joint propul conf (Arizona, USA). AIAA 2005-4301; 2005.
- [5] Pizzarelli M, Nasuti F, Paciorni R, Onofri M. Numerical analysis of three-dimensional flow of supercritical fluid in asymmetrically heated channels. AIAA J 2009;47:2534–43.
- [6] Pizzarelli M, Nasuti F, Onofri M. Analysis of curved-cooling-channel flow and heat transfer in rocket engines. J Propul Power 2011;27:1045–53.
- [7] Coleman GN, Kim J, Moser RR. A numerical study of turbulent supersonic isothermal channel flow. J Fluid Mech 1995;305:159–83.
- [8] Kim D, Jang HK. Very large-scale motion in the outer layer. Phys Fluids 1999;11:417–22.
- [9] Ringuette MJ, Wu M, Martin MP. Coherent structures in DNS of turbulent boundary layers at Mach 3. J Fluid Mech 2008;594:59–69.
- [10] Taieb D, Ribert G. DNS and LES of supersonic channel flow with isothermal walls. J Propul Power 2013;29(5):1064–75.
- [11] Locke J, Landrum D. Study of heat transfer correlations for supercritical hydrogen in regenerative cooling channels. J Propul Power 2008;24:94–103.
- [12] Pioro I, Khartabil H, Duffey R. Heat transfer to supercritical fluids flowing in channels – empirical correlations (survey). Nucl Eng Des 2004;230:69–91.
- [13] Cheng X, Kuang B, Yang Y. Numerical analysis of heat transfer in supercritical water cooled flow channels. Nucl Eng Des 2007;237:240–52.
- [14] Yang V. Modeling of supercritical vaporization, mixing, and combustion processes in liquid-fueled propulsion systems. Proc Combust Inst 2000;28:925–42.
- [15] Meng H, Yang V. A unified treatment of general fluid thermodynamics and its application to a preconditioning scheme. J Comput Phys 2003;189:277–304.
- [16] Hsieh S, Yang V. A preconditioned flux-differencing scheme for chemically reacting flows at all Mach numbers. Int J Comput Fluid Dyn 1997;8:31–49.
- [17] Oefelein J, Yang V. Modeling high-pressure mixing and combustion processes in liquid rocket engines. J Propul Power 1998;14:843–57.
- [18] Ribert G, Zong N, Yang V, Pons L, Darabiha N, Candel S. Counterflow diffusion flames of general fluids: oxygen/hydrogen mixtures. Combust Flame 2008;154:319–30.
- [19] Zong N, Yang V. An efficient preconditioning scheme for general fluid mixture using primitive variables. Int J Comput Fluid Dyn 2007;21:217–30.
- [20] Li H-G, Zong N, Lu X-Y, Yang V. A consistent characteristic boundary condition for general fluid mixture and its implementation in a preconditioning scheme. Adv Appl Math Mech 2012;4:72–92.
- [21] Swanson R, Turkel E. On central difference and upwind schemes. J Comput Phys 1992;101:292–306.
- [22] Jiang G, Shu C. Efficient implementation of weighted ENO schemes. J Comput Phys 1996;126:202–28.
- [23] Martin MP, Taylor EM, Wu M, Weirs VG. A bandwidth-optimized WENO scheme for effective direct numerical simulation of compressible turbulence. J Comput Phys 2006;220:270–89.
- [24] Taylor EM, Wu M, Martin MP. Optimization of nonlinear error for weighted essentially non-oscillatory methods in direct numerical simulations of compressible turbulence. J Comput Phys 2007;223:384–97.
- [25] Taieb D, Ribert G, Hadjadj A. Numerical simulations of shock focusing over concave surfaces. AIAA J 2010;48:1739–47.
- [26] Graboski M, Daubert T. A modified Soave equation of state for phase equilibrium calculation, 1. Hydrocarbon systems. Ind Eng Chem Proc Des Devel 1978;17:443.
- [27] Graboski M, Daubert T. A modified Soave equation of state for phase equilibrium calculation, 2. Systems containing CO<sub>2</sub>, H<sub>2</sub>S, N<sub>2</sub>, and CO. Ind Eng Chem Proc Des Devel 1978;17:448.
- [28] Chung T, Ajlan M, Lee L, Starling K. Generalized multiparameter corresponding state correlation for polyatomic, polar fluid transport properties. Ind Chem Eng Res 1988;27:671–9.
- [29] Quering K, Zeiss W, Wiedmann D, Knab O, Torres Y, Suslov D. Numerical and experimental studies of heat transfer in asymmetrically heated cooling channels. In: 3rd European conf for aero sci (EUCASS); 2009.
- [30] Torres Y. Heat and mass transfer in curvatures of cooling channels of rocket engine. Ph.D. thesis. France: University of Valenciennes; 2008.
- [31] Torres Y, Suslov D, Haidn O. Nitrogen two-phases in regenerative cooling channels of rocket engine. In: 3rd European conf for aero sci (EUCASS); 2009.
- [32] Ribert G, Taieb D, Petit X, Lartigue G, Domingo P. Simulation of supercritical flows in rocket-motor engines: application to cooling channel and injection

- system, Eucass Book Series. Adv Aerospace Sci, Prog Propul Phys 2012;4:661–82.
- [33] Poinot T, Lele S. Boundary conditions for direct simulations of compressible viscous flows. *J Comput Phys* 1992;101:104–29.
- [34] Zong N, Meng H, Hsieh S-Y, Yang V. A numerical study of cryogenic fluid injection and mixing under supercritical conditions. *Phys Fluids* 2004;16(12):4248.
- [35] Klein M, Sadiki A, Janicka J. A digital filter based generation of inflow data for spatially developing direct numerical or large eddy simulations. *J Comput Phys* 2003;186:652–65.
- [36] Smagorinsky J. General circulation experiments with the primitive equations. *Mon Weather Rev* 1963;91:99–164.
- [37] Jimenez J, Moin P. The minimal flow unit in near-wall turbulence. *J Fluid Mech* 1991;225:213–40.
- [38] Morkovin M. Effects of compressibility on turbulent flows. In: Favre A, editor. London: Gordon and Breach; 1990.
- [39] Gaviglio J. Reynolds analogies and experimental study of heat transfer in supersonic boundary layer. *Int J Heat Mass Transfer* 1987;30:911–26.
- [40] Rubesin M. Extra compressibility terms for Favre-averaged two-equation models of inhomogeneous turbulent flows. NASA CR-177556; 1990.
- [41] Huang P, Coleman G, Bradshaw P. Turbulence statistics in fully developed channel flow at low reynolds number. *J Fluid Mech* 1995;177:133–66.
- [42] Brun C, Petrovan Boiarciuc M, Haberkorn M, Comte P. Large eddy simulation of compressible channel flow. *Theor Comput Fluid Dyn* 2008;22:189–212.
- [43] Petit X, Ribert G, Lartigue G, Domingo P. Large-eddy simulation of supercritical fluid injection. *J Supercrit Fluids* 2013;84:61–73.
- [44] Petit X, Ribert G, Domingo P. Framework for real-gas compressible reacting flows with tabulated thermochemistry. *J Supercrit Fluids* 2015;101:1–16.